



# Robust subsynchronous interaction damping controller for DFIG-based wind farms



Mohsen GHAFOURI<sup>1</sup>, Ulas KARAAGAC<sup>2</sup> , Houshang KARIMI<sup>1</sup>,  
Jean MAHSEREDJIAN<sup>1</sup>

**Abstract** This paper proposes a robust controller to improve power system stability and mitigate subsynchronous interaction (SSI) between doubly-fed induction generator (DFIG)-based wind farms and series compensated transmission lines. A robust stability analysis is first carried out to show the impact of uncertainties on the SSI phenomenon. The uncertainties are mainly due to the changes in the power system impedance (e.g., transmission line outages) and the variations of wind farm operating conditions. Then, using the  $\mu$ -synthesis technique, a robust SSI damping controller is designed and augmented to the DFIG control system to effectively damp the SSI oscillations. The output signals of the supplementary controller are dynamically limited to avoid saturating the converters and to provide DFIG with the desired fault-ride-through (FRT) operation during power system faults. The proposed controller is designed for a realistic test system with multiple series capacitor compensated lines. The frequency of

the unstable SSI mode varies over a wide range due to the changes in power system topologies and wind farm operating conditions. The performance of the proposed controller is verified through electromagnetic transient (EMT) simulations using a detailed wind farm model. Simulation results also confirm the grid compliant operation of the DFIG.

**Keywords** Doubly-fed induction generator (DFIG), Subsynchronous interaction (SSI),  $\mu$ -synthesis, Robust control, Series capacitor compensation

## 1 Introduction

Modern large-scale wind farms employ variable-speed wind turbines (WTs) in order to increase energy capture, reduce drive train stresses and comply with the grid code requirements. Doubly-fed induction generator (DFIG) and full rated converter (FRC) WTs fall into this category. However, FRC WTs have cost disadvantages [1].

DFIGs may be exposed to subsynchronous interaction (SSI) phenomenon, in particular, when they are radially connected to a series compensated transmission line [2]. This phenomenon was first reported in the Electric Reliability Council of Texas (ERCOT) power system [3, 4] in 2009. Since then, various studies have been conducted to investigate and propose methods for mitigating such phenomenon [5]. Among the existing methods, adding supplementary SSI damping controller into DFIG control loops is a promising approach due to its low cost and simple structure [6–12]. The promising control schemes are based on the usage of lead-lag compensator [7], partial feedback linearization (PFL) [8], linear quadratic regulator (LQR) [9, 10], low-pass filter with phase compensation

CrossCheck date: 13 February 2019

Received: 16 November 2018 / Accepted: 13 February 2019 /  
Published online: 1 October 2019

© The Author(s) 2019

✉ Ulas KARAAGAC  
ulas.karaagac@polyu.edu.hk

Mohsen GHAFOURI  
Mohsen.Ghafouri@polymtl.ca

Houshang KARIMI  
Houshang.Karimi@polymtl.ca

Jean MAHSEREDJIAN  
jean.mahseredjian@polymtl.ca

<sup>1</sup> Department of Electrical Engineering, Polytechnique Montreal, Montreal H3T 1J4, Canada

<sup>2</sup> Department of Electrical Engineering, The Hong Kong Polytechnic University, Hong Kong, China



[11] and proportional-integral (PI) supplementary controller [12]. However, some important issues, such as realistic wind farm model, variation of power system parameters and the transient behavior of the system against the faults should be investigated to conclude on effectiveness of those methods. Therefore, [9, 10] consider a wind farm with a realistic reactive power control scheme and design the SSI damping controller considering the potential negative impact on the WT transient response during faults.

The existing literatures only consider the wind farms connected to power systems with a single series capacitor compensated line. In such a system, the frequency change of unstable SSI mode is limited as it is mainly due to the variation of wind farm operation conditions, such as wind speed and WT outages. On the other hand, the frequency of the unstable SSI mode can be expected to vary over a wide range due to the contingencies in power transmission system when it is connected through multiple series capacitor compensated lines. This paper proposes a robust controller based on  $\mu$ -synthesis technique [13, 14] to tackle the problem of SSI between a DFIG-based wind farm and a power system with multiple series capacitor compensated lines. In the design procedure, the uncertain power system is modeled with a series RLC branch whose parameters can vary in a certain range. To show the impact of power system uncertainties and wind farm operation conditions in the SSI modes, a comprehensive robust stability analysis is performed based on eigenvalue and sensitivity analysis.

The designed controller uses the currents of the rotor side converter (RSC) and grid side converter (GSC) in  $dq$ -frame as its input vector. The supplementary control signals are dynamically limited to avoid saturating the converters and to provide the DFIG with the desired transient response against power system faults [9, 10]. Furthermore, the proposed controller does not require any communication links between WTs and the wind farm secondary control layer as it only uses the measurements available at each DFIG. Hence, its implementation does not introduce any additional challenges [10].

The effectiveness of the proposed controller is verified using electromagnetic transient (EMT) simulations for a realistic power system with multiple series capacitor compensated lines. The frequency of the SSI mode changes significantly at each line outage scenario. The wind farm EMT model in [9, 10] is used in this research. The model has a realistic reactive power control scheme and the fault-ride-through (FRT) function which is essential for grid compliant operation.

The paper is organized as follows. Section 2 briefly describes the structure of wind farm and its modeling. Section 3 presents the system under study. The robust stability analysis is presented in Section 4. Section 5

presents the controller design procedure and the design limitation/considerations. EMT simulation results are presented in the Section 6.

## 2 Wind farm modeling

Figure 1 depicts the simplified schematic diagram of a radially compensated DFIG-based wind farm used in eigenvalue analysis. The equivalent system seen from DFIG low voltage terminal is represented by a series RLC branch behind a constant voltage at fundamental frequency. The DFIG is represented with its linearized model [9]. The simplification in linearized DFIG model enables straightforward analysis and low-order controller design. On the other hand, the obtained results remain conservative by disregarding the low-pass measuring filters and phase locking loop (PLL) dynamics [15].

The simplified schematic diagram of RSC and GSC is shown in Fig. 2. The control of RSC and GSC is based on the vector control technique. The GSC and RSC signals are transferred to the stator voltage and flux reference frames, respectively.  $i_{qg}$  and  $i_{dg}$  are the  $q$ -axis and  $d$ -axis currents of the GSC;  $v_{qg}$  and  $v_{dg}$  are the  $q$ -axis and  $d$ -axis voltages of the GSC;  $V_{DC}$  is the DC bus voltage;  $P_{DFIG}$  is the DFIG active power output;  $V_{DFIG}$  is the DFIG positive sequence terminal voltage;  $i_{qr}$  and  $i_{dr}$  are  $q$ -axis and  $d$ -axis currents of RSC;  $v_{qr}$  and  $v_{dr}$  are  $q$ -axis and  $d$ -axis voltages of RSC; and  $\omega_{mech}$  is the mechanical speed of DFIG rotor. The primed variables are used to indicate reference values.

The RSC outer controls are utilized to control the DFIG positive sequence voltage ( $V_{DFIG}$ ) and active power ( $P_{DFIG}$ ). The reference value for the DFIG active power is obtained from the maximum power point tracking (MPPT) block and the DFIG positive sequence voltage reference in Fig. 2 is produced by the wind farm controller (WFC). The GSC  $d$ -axis current is used to regulate the DC link voltage, whereas its  $q$ -axis current is utilized to support the grid voltage during faults. In normal operation of the DFIG,  $i'_{qg}$  is zero and consequently the GSC operates at unity power factor.

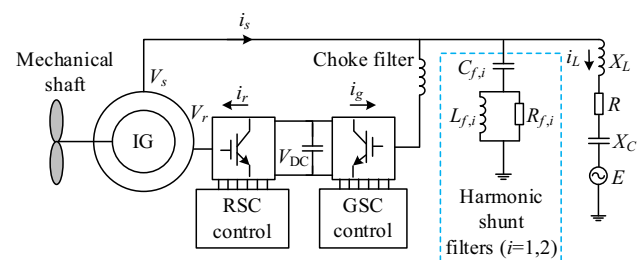


Fig. 1 Radially compensated wind farm model used in eigenvalue analysis

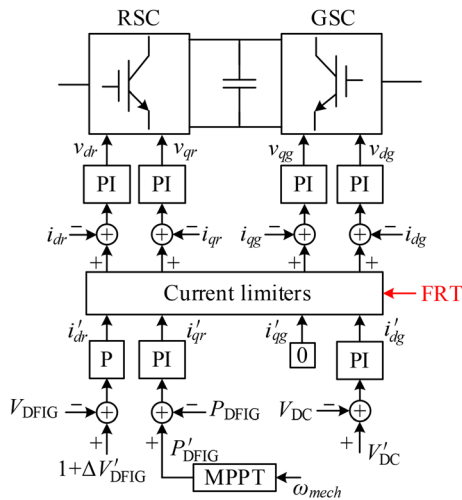


Fig. 2 Control scheme of DFIG converters

The reactive power at point of interconnection (POI) is controlled by two control levels. At primary level, WT controller (WTC) regulates its own positive sequence terminal voltage using a proportional voltage regulator ( $K_v$ ) as shown in Fig. 2. At secondary level, WFC controls the reactive power at POI ( $Q_{POI}$ ) by modifying the WTC reference voltage ( $1 + \Delta V'_{DFIG}$ ) through a PI reactive power regulator. This operation of the WFC (called  $Q$ -control) is detailed in [9]. The WFC may also contain voltage control and power factor control functions. Please refer to [16] for more details. This paper considers WFC operating under  $Q$ -control.

The grid code requirements include the WT transient response against the severe voltage sag or swell conditions [17]. An FRT function is traditionally added to WTC to comply with this requirement. A severe change in WT terminal voltage activates the FRT function to supply the desired reactive currents defined in the grid code. This paper considers a DFIG-based WT that has an FRT function compliant with the requirement described in [17].

### 3 System under study

To evaluate the effectiveness of the proposed SSI mitigation method, the system shown in Fig. 3 is adopted as a test benchmark. The wind farm consists of 266 DFIG-based WTs of 1.5 MW. It is connected to the power system (represented by Thevenin equivalents) through 500 kV transmission lines A, B and C with the lengths of 100 km, 500 km and 700 km, respectively. Transmission lines B and C are compensated with 50% compensation level using identical capacitor banks at their ends. In Fig. 3,  $B_1$ ,  $\bar{B}_1$ ,  $B_2$ ,  $\bar{B}_2$ ,  $B_3$  and  $\bar{B}_3$  are the line circuit breakers.

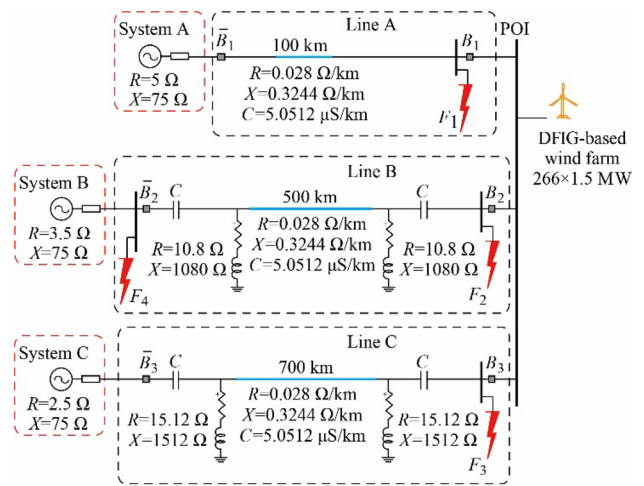


Fig. 3 Test system under study

The SSI prediction can be done with the combined frequency scan analysis of the power system and WT [15]. The combined frequency scans for no line outage, outage of line A, outages of lines A and B, and outages of lines A and C are presented in Figs. 4, 5, 6 and 7, respectively. In these figures,  $R_T$  and  $X_T$  are the total resistance and reactance of the combined scan analysis; and  $W$  is the per-unit wind speed on 11.24 m/s (rated wind speed) base. As shown in Fig. 4, there is no reactance crossover and consequently no possibility of SSI in no line outage scenario. On the other hand, depending on both wind speed and transmission line outage scenario, the system has several reactance crossovers with 25.0–30.5 Hz frequency range, as shown in Figs. 5, 6 and 7. The total resistance is negative (i.e. the system is unstable) in those scenarios. It should be noted that this frequency range becomes much wider when the WT outage scenarios are considered.

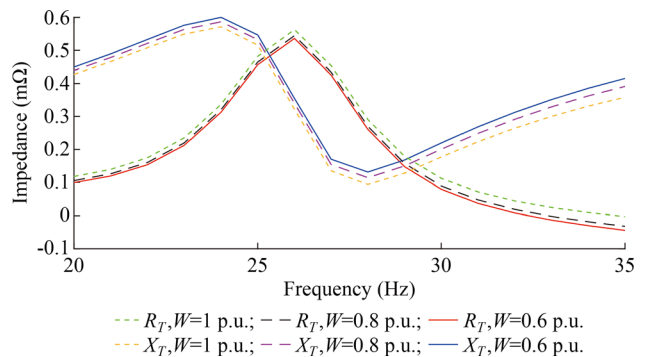
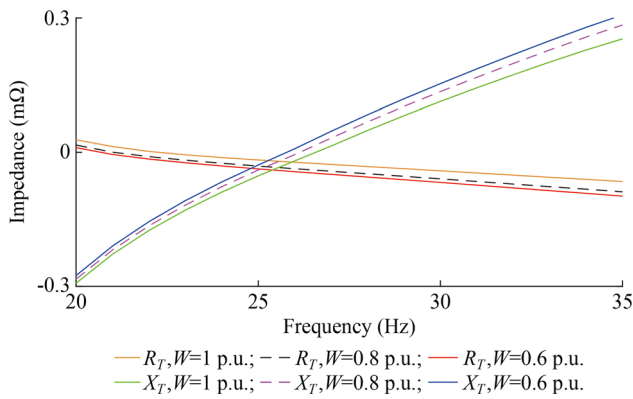
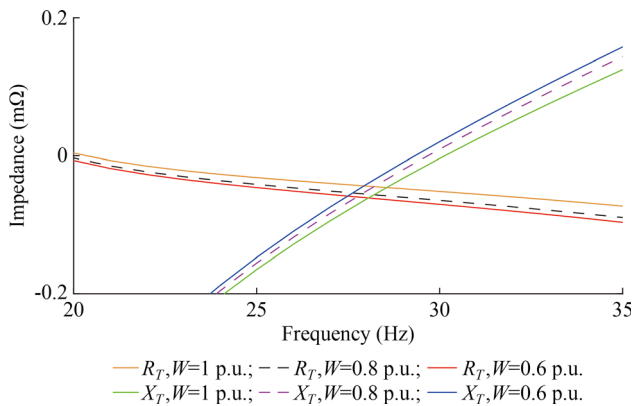


Fig. 4 Combined frequency scan for various wind speeds and no line outage scenario



**Fig. 5** Combined frequency scan for various wind speeds and line A outage scenario



**Fig. 6** Combined frequency scan for various wind speeds and lines A and B outage scenario

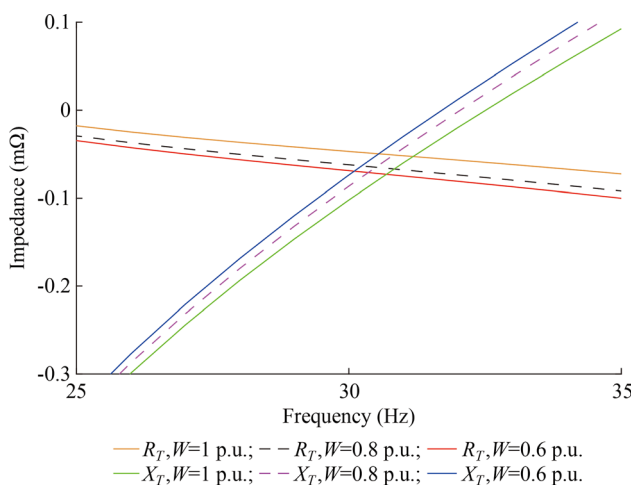


**Fig. 7** Combined frequency scan for various wind speeds and lines A and C outage scenario

#### 4 Robust stability analysis

The robust stability analysis and controller design are performed using the simplified linear model of the system. The state-space representation of the system can be expressed as:

$$\begin{cases} \dot{x} = Ax + Bu \\ y = Cx + Du \end{cases} \quad (1)$$

where  $x$ ,  $u$  and  $y$  are the vectors of the system states, inputs, and outputs, respectively. The matrices  $A$ ,  $B$ ,  $C$  and  $D$  are obtained from linearization procedure and specify the small-signal behavior of the system. The details of linearization process can be found in [9].

In eigenvalue analysis and SSI damping controller design, the external system seen from the aggregated DFIG-based WT is represented with a simple series RLC circuit and a fundamental frequency voltage source as shown in Fig. 1. The line outage scenarios which are potentially susceptible to SSI problem (i.e. the line outage scenarios presented in Figs. 5, 6 and 7) are considered. At each line outage scenario, the fundamental and subsynchronous frequency characteristics of the external system can be approximated with a reasonable accuracy by adjusting the series RLC circuit parameters ( $R$ ,  $X_L$  and  $X_C$  in Fig. 1). The following range covers the variations in RLC circuit parameters for the considered line outage scenarios:

$$\begin{cases} 0.020 < R < 0.035 & R_0 = 0.029 \\ 0.40 < X_L < 0.52 & X_{L,0} = 0.45 \\ 0.05 < X_C < 0.07 & X_{C,0} = 0.06 \end{cases} \quad (2)$$

where the parameters indicated by the “0” subscript represent the equivalent system impedance when the wind farm is connected only to line B, i.e. line outage scenario shown in Fig. 7. To obtain these ranges, all outage scenarios and variations of the system parameters are considered, and the system impedance is calculated accordingly. These ranges represent a cube in the uncertainty space. When an extremely wide uncertainty range is considered during design, this will result in a conservative design of controller and a deterioration in its performance.

Figures 8, 9 and 10 show the sensitivity of the SSI mode to the variations in system equivalent resistance, reactance and capacitance ( $R$ ,  $X_L$  and  $X_C$  in Fig. 1) for different wind speeds. Each curve is plotted for a specific wind speed (from  $W = 0.6$  p.u. to  $W = 1$  p.u.). The values of the SSI modes shown in Figs. 8–10 can be found in Appendix A.

The increase of  $R$  results in a decrease of the SSI frequency and an increase in the damping of the SSI mode. The increase in  $X_L$  results in the damping and frequency of the larger SSI mode. The increase in  $X_C$  results in the damping and frequency of the lower SSI mode. The presented results in Figs. 8, 9 and 10 and Tables A1–A3 of Appendix A also demonstrate that the system becomes more vulnerable to SSI at slower wind speeds.



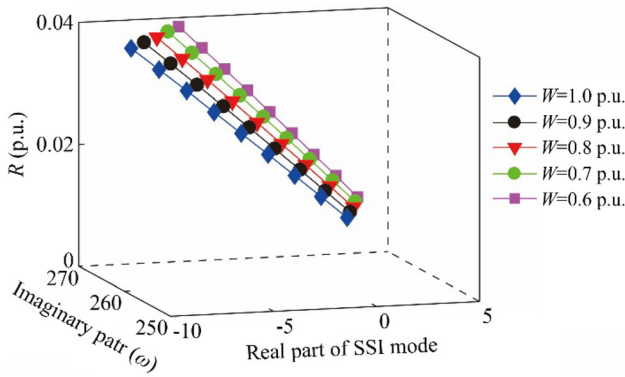


Fig. 8 Impact of variations in  $R$  and wind speed on SSI mode

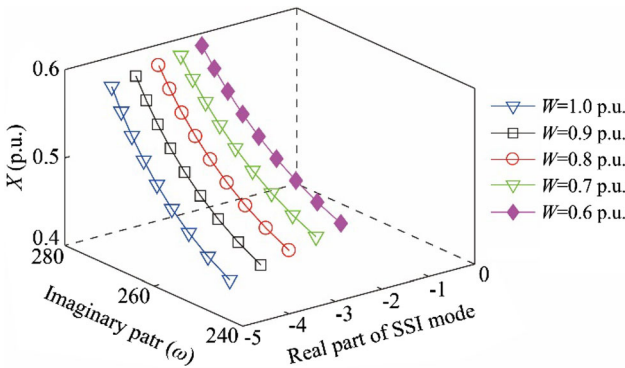


Fig. 9 Impact of variations in  $X_L$  and wind speed on SSI mode

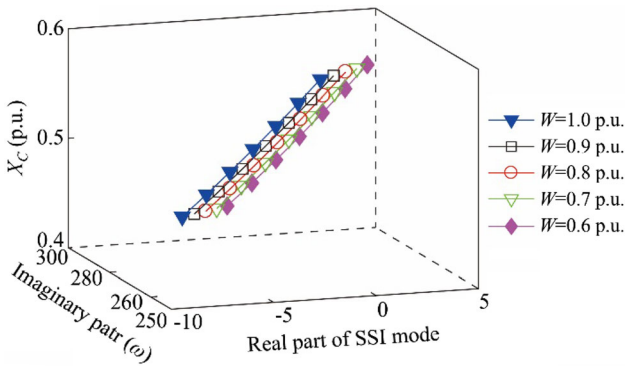


Fig. 10 Impact of variations in  $X_C$  and wind speed on SSI mode

The impact of WT outages inside the wind farm is demonstrated in Fig. 11 and Table A4 of Appendix A. The damping of the SSI mode is smallest when there are 150 WTs in service inside the wind farm.

The WT control parameters also have significant impact on the damping of the SSI mode [9, 15]. On the other hand, the WT parameters are set by the manufacturer and do not change during the operation. Hence, their variations are not considered in the controller design.

Figure 12 illustrates the linear fractional transformation (LFT) of the system, where  $P$  is the simplified open-loop

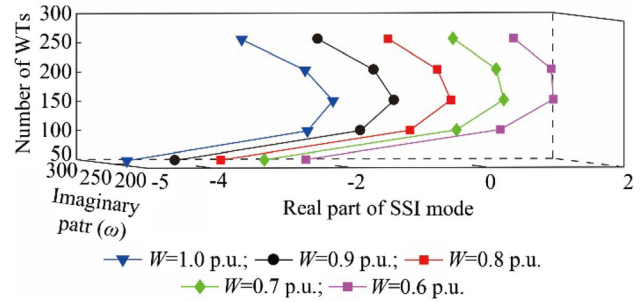


Fig. 11 Impact of WT outages and wind speed on SSI mode

model used to design the controller and perform the robust analysis;  $u_\Delta$  and  $y_\Delta$  are the inputs and outputs of the uncertainty block. The input vector  $w$  contains the exogenous signals such as references and disturbances, and  $Z$  is the signals with meaning of error used to characterize the system performance. The uncertainties are augmented into the block  $\Delta$  which is defined as:

$$\Delta = \text{diag}[\delta_1 I_{r_1}, \dots, \delta_s I_{r_s}, \Delta_1, \dots, \Delta_f] \tag{3}$$

$$\begin{cases} \delta_i \in \mathcal{C} \\ \Delta_f \in \mathcal{C}^{m_j \times m_j} \\ \sum_{i=1}^s r_i + \sum_{j=1}^f m_j = n \end{cases} \tag{4}$$

where  $n$  is dimension of  $\Delta$ ;  $I_{r_i}$  is  $r_i \times r_i$  identity matrix;  $\delta_i$  denotes the parametric uncertainty as described in (2). Figure 13 shows the singular values of the system for 10 uniformly chosen uncertainties in  $R$ ,  $X_L$  and  $X_C$ . The worst-case scenario (most severe oscillations) occurs when  $R$ ,  $X_L$  and  $X_C$  are 0.0281, 0.4034 and 0.07 p.u., respectively. In this scenario, the frequency of SSI oscillations is 41 Hz shown in Fig. 13.

The structured singular value  $\mu_\Delta(P)$  is the smallest singular value of matrix  $\Delta(\sigma(\Delta))$  for which  $I - P\Delta$  is singular, i.e.,

$$\mu_\Delta^{-1} = \min_{\Delta \in \Lambda} \{\bar{\sigma}(\Delta) : \det(I - P\Delta) = 0\} \tag{5}$$

It is also assumed that if there is no  $\Delta \in \Lambda$  for which  $\det(I - P\Delta) = 0$ , then  $\mu_\Delta(P) = 0$ .

The open-loop system ( $P$ ) is robustly stable with respect to  $\Delta(\|\Delta\|_\infty < \beta)$  if and only if  $P$  is stable and  $\mu_\Delta(P) < 1/\beta$ .

The lower and upper bounds of the stability margin are 0.4141 and 0.7952, respectively. The family of the open-loop systems is not stable, in particular, when the

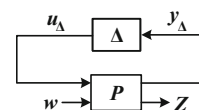


Fig. 12 Linear fractional transformation of system

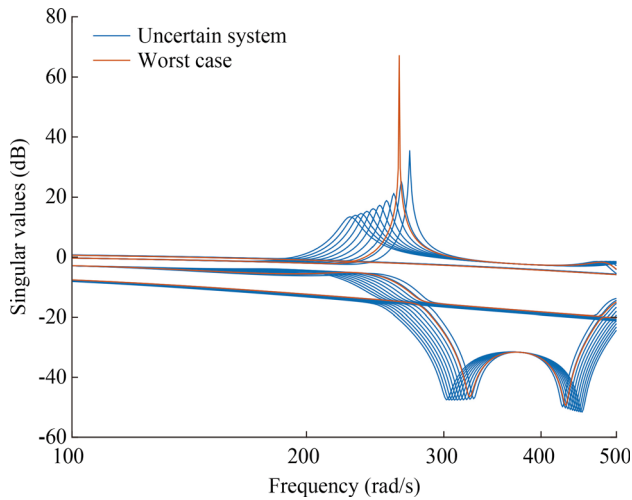


Fig. 13 Singular values of the uncertain system

parameters exceed their nominal values by 41.4%. Increasing  $R$ ,  $X_L$  and  $X_C$  by 25% results in 4%, 3% and 9% decrease in the stability margin, respectively.

The open-loop system with its conventional controllers does not satisfy reference tracking and disturbance rejection for all uncertain parameters, i.e., it does not provide robust performance. The lower and upper bounds of the performance are 0.0549 and 0.0556, respectively. The 25% increase in  $R$ ,  $X_L$  and  $X_C$  will result in 1%, 2%, and 2% decrease in the performance margins, respectively. The upper and lower bounds of  $\mu$  are shown in Fig. 14. The upper bound for  $\mu$  is the maximum singular value of the matrix  $P$  and its lower bound is the spectral radius of this matrix. As the upper bound of  $\mu$  exceeds 1 over a frequency range, the system is not robustly stable.

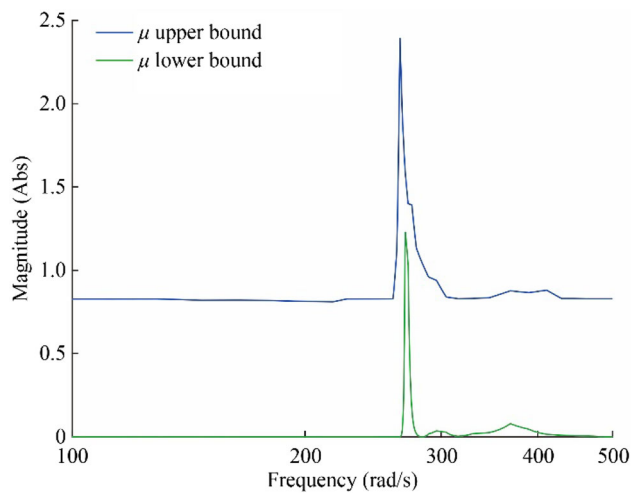


Fig. 14 Upper and lower bounds of  $\mu$  in the open-loop system

### 5 $\mu$ -controller design

Figure 15 shows the standard  $M - \Delta$  control design schematic diagram. The controller model is denoted by  $K$ .

The family of plants can be expressed as:

$$\begin{cases} F_u(P, \Delta) : \Delta \in \Delta \\ \max_{\omega} \bar{\sigma}(\Delta(j\omega)) \leq 1 \end{cases} \quad (6)$$

The controller  $K$  should stabilize the plant for all  $\Delta \in \Delta$ .  $\mu$ -synthesis technique minimizes the peak of the structured singular value of  $F_u(P, K)$  over the set of all stabilizing controllers ( $\Omega$ ), i.e.

$$\min_{K \in \Omega} \max_{\omega} \mu_{\Delta_p}(F_u(P, K)(j\omega)) \quad (7)$$

The control scheme of the system is illustrated in Fig. 16, where vectors  $d$ ,  $r$  and  $Z = [Z_1 \ Z_2]^T$  are the disturbance, reference and error output, respectively; and  $G$  is the nominal system.

The design goal is to achieve the robust stability and robust performance for the following family of uncertain systems.

$$\begin{cases} Z = T_{Zw}w \\ Z = \begin{bmatrix} Z_1 \\ Z_2 \end{bmatrix} \\ w = \begin{bmatrix} r \\ d \end{bmatrix} \end{cases} \quad (8)$$

where  $T_{Zw}$  is the transfer function that describes the relation between the  $w$  and  $Z$ .

The details of the criteria which need to be satisfied can be found in [18–20]. The weighting functions are used to shape the frequency response of the closed-loop system shown in Fig. 16.  $W_p$  is a low-pass filter used to reject the disturbances in low frequency range.  $W_u$  is a high-pass filter which minimizes the control effort and rejects the switching harmonics of the converters. The guidelines for designing these filters are presented in [18, 19]. In this paper, the objective is to reject the disturbances below 5 Hz, and to attenuate the switching frequencies of RSC ( $f_{sw} = 2250$  Hz) and GSC ( $f_{sw} = 4500$  Hz). Therefore, the weighting matrices are obtained as below:

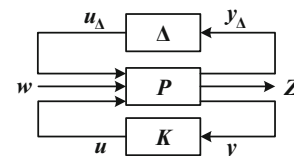


Fig. 15 Standard  $M - \Delta$  configuration for controller design

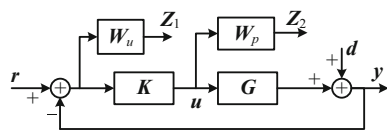


Fig. 16 Block diagram of closed-loop system for controller design

$$\begin{cases} W_x = \begin{pmatrix} W_x & 0 & 0 & 0 \\ 0 & W_x & 0 & 0 \\ 0 & 0 & W_x & 0 \\ 0 & 0 & 0 & W_x \end{pmatrix} & x = p, u \\ W_p = \frac{0.01(s + 10)}{(s + 2\pi(5))} \\ W_u = \frac{0.1(0.001s + 1)}{(0.0001s + 1)} \end{cases} \quad (9)$$

The *DK*-iteration method is used to compute the controller parameters using Robust Control Toolbox in MATLAB. *DK*-iteration technique is an iterative optimization method used to calculate the value of  $\mu$  and controller parameters. The calculation of  $\mu$  is a challenging task, whereas its upper and lower bounds can be computed easily. Therefore, a transformation matrix  $D(s)$  is used to narrow the distance between the upper and lower bounds of  $\mu$  while keeping its value fixed. In *DK*-iteration technique, an initial value is considered for  $D(s)$  (often  $D(s) = I$ ). Then, using this matrix the controller  $K(s)$  is computed by solving an  $H^\infty$  optimization. In the next step, assuming the fixed  $K(s)$  controller,  $D(s)$  is updated at each frequency over the considered frequency range. The updated  $D(s)$  is then curve fitted to obtain a stable and minimum-phase transformation. This procedure is repeated until a prespecified convergence tolerance is achieved for (7). The details of this technique can be found in [20]. The order of the designed controller is then reduced using Hankel singular value (HSV) approach [20]. The HSVs show the amount of energy in the states of the system. Fig. 17 shows that reducing controller order to 6 will not affect its performance. Fig. 18 illustrates the lower and upper bounds of  $\mu$ , which also shows a reduction in the peak value of  $\mu$  to below 1. It should be noted that the bounds of  $\mu$  are calculated using the closed-loop system matrix as shown in Fig. 15.

### 6 EMT simulations

Table 1 presents the simulation scenarios. The simulation step time is 50  $\mu$ s. The simulations are performed using EMTP [21] and the generic wind farm model in [16, 22]. The fault locations  $F_1$ – $F_4$  are illustrated in Fig. 3. Three-phase metallic fault is applied at  $t = 1$  s in scenarios S1–S6 (i.e. at  $F_1$ – $F_3$ ). The faults  $F_1$ ,  $F_2$  and  $F_3$  take place in

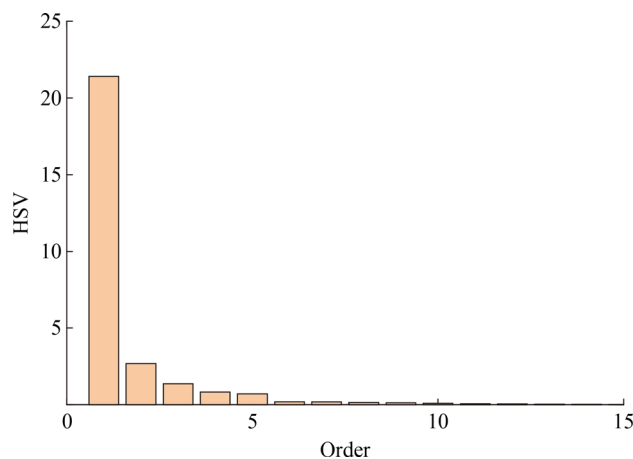


Fig. 17 HSVs of controller

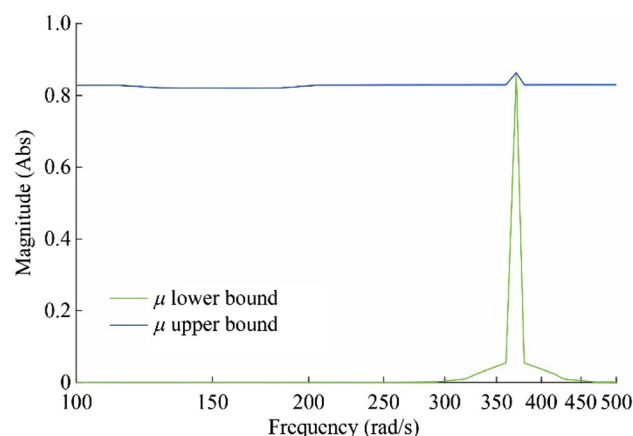


Fig. 18 Upper and lower bounds of  $\mu$  in closed-loop system

Table 1 Simulation scenarios

Scenario	Fault location	Line outage (prior to fault)	WT outage (prior to fault)	SSI damping control
S1	$F_1$	No outage	No outage	Out of service
S2	$F_1$	No outage	No outage	In service
S3	$F_2$	Line A	No outage	Out of service
S4	$F_2$	Line A	No outage	In service
S5	$F_3$	Line A	34×4 WTs	Out of service
S6	$F_3$	Line A	34×4 WTs	In service
S7	$F_4$	Line A	No outage	Out of service
S8	$F_4$	Line A	No outage	In service

the wind farm at the end of the transmission lines A, B and C, respectively. Those faults are cleared with the operation of the line circuit breakers. The close and remote breakers



operate in 60 ms and 80 ms, respectively. On the other hand, the three-phase fault  $F_4$  in scenario S7 and S8 takes place at the terminal of the Thevenin source of the equivalent system B shown in Fig. 3. The fault impedance is  $0.3162 \Omega$  and  $X/R = 3$ . This fault is cleared with the operation of the equivalent system B end circuit breaker of the line after 300 ms. This fault scenario imitates a fault inside the equivalent system B and its clearance with the operation of the backup protection (such as due to breaker failure) which involves the breakers of the busbar to which transmission line B is connected. It should be noted that S7 and S8 are repeated for different type of faults as well as system impedances that result 0.5 to 0.8 voltage sag at DFIG terminals. However, these results are not presented in the paper due to the similar performance of controller and space limitations. In all the scenarios, wind speed is 0.6 p.u. (i.e. the permissible slowest wind speed) and there are no WT outages inside the wind farm.

Figures 19, 20, 21 and 22 show the active and reactive powers delivered by the aggregated WT for the scenarios S1–S8. The system is unstable without SSI damping controller in all scenarios and the frequency of SSI mode is the same as those obtained through the frequency scan and eigenvalue analysis. The simulation results presented in those figures also confirm the effectiveness of the proposed SSI damping controller. The utilized  $\mu$ -synthesis technique stabilizes the system in all scenarios regardless of dramatic differences between the frequencies of the SSI mode and initial damping. Although the SSI mode has negative damping during fault in scenarios S7 and S8 shown in Fig. 22, the system remains stable after fault clearance with the proposed mitigation.

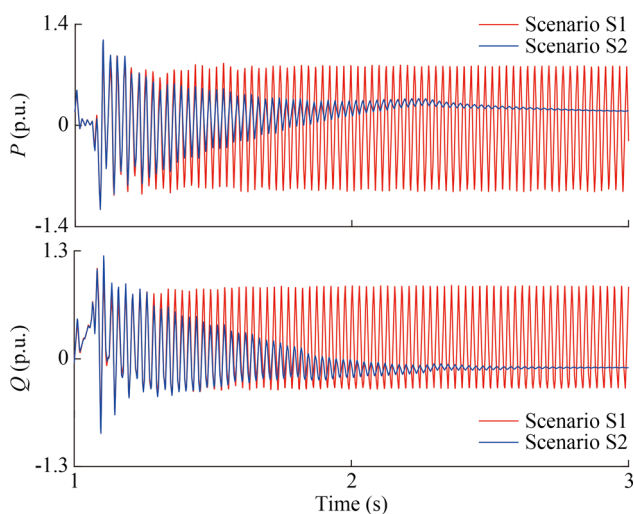


**Fig. 19** Active and reactive power components of the aggregated WT in scenarios S1 and S2

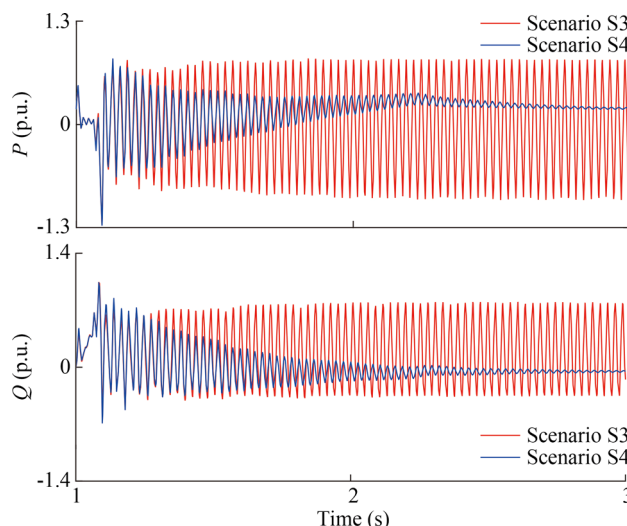


**Fig. 20** Active and reactive power components of the aggregated WT in scenarios S3 and S4

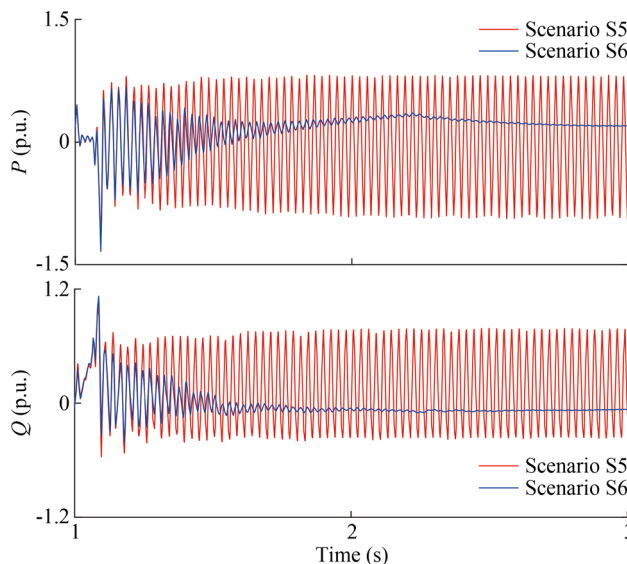


**Fig. 21** Active and reactive power components of the aggregated WT in scenarios S5 and S6

As shown in Fig. 11, the system becomes most vulnerable to SSI when there are 150 WTs in service. To demonstrate the effectiveness of the proposed damping controller in such extreme WT outage conditions, the scenarios S2, S4, S6 and S8 are repeated for the case in which 150 WTs are in service in wind farm. Those simulation scenarios are indicated with “\*” sign. The presented results in Fig. 23 show that the proposed damping controller stabilizes the system effectively in those WT outage scenarios as well.



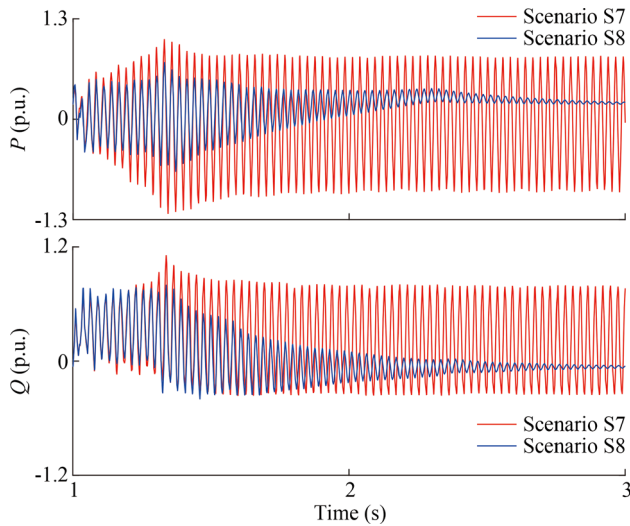


**Fig. 22** Active and reactive power components of the aggregated WT in scenarios S7 and S8

In order to demonstrate the effectiveness of the proposed controller for higher wind speeds, the scenarios S2, S4, S6 and S8 are also repeated for wind speeds of 0.8 p.u. and 1.0

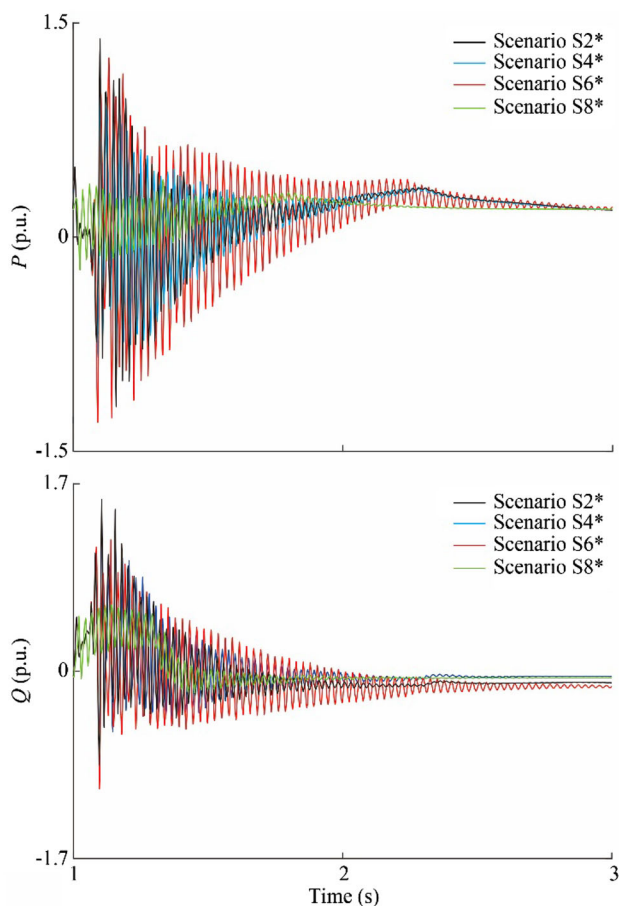


**Fig. 23** Active and reactive power components of the aggregated WT in scenarios S2\*, S4\*, S6\* and S8\*

p.u.. The results are presented in Figs. 24 and 25. The simulation scenarios are indicated with “\*\*” and “\*\*\*” signs for 0.8 p.u. and 1.0 p.u. wind speeds, respectively.

### 7 Conclusion

In this paper, based on the  $\mu$ -synthesis technique, a robust controller is proposed to damp the SSI oscillations in series compensated wind farms with DFIGs. The proposed damping controller is designed for a realistic test system with multiple series capacitor compensated lines in which the frequency of the unstable SSI mode changes in a wide range with the transmission line outages and wind farm operating conditions.

A simple linearized system is used for the analysis of SSI phenomenon and controller synthesis. Although the collector grid and the DFIGs inside the wind farm are represented with their aggregated models, the central WFC is also considered to preserve the overall reactive power control structure inside the wind farm.

The effectiveness of the proposed damping controller is validated through EMT simulations. The EMT model of DFIG includes all the nonlinearities (in both electrical and control system model) and essential transient functions to

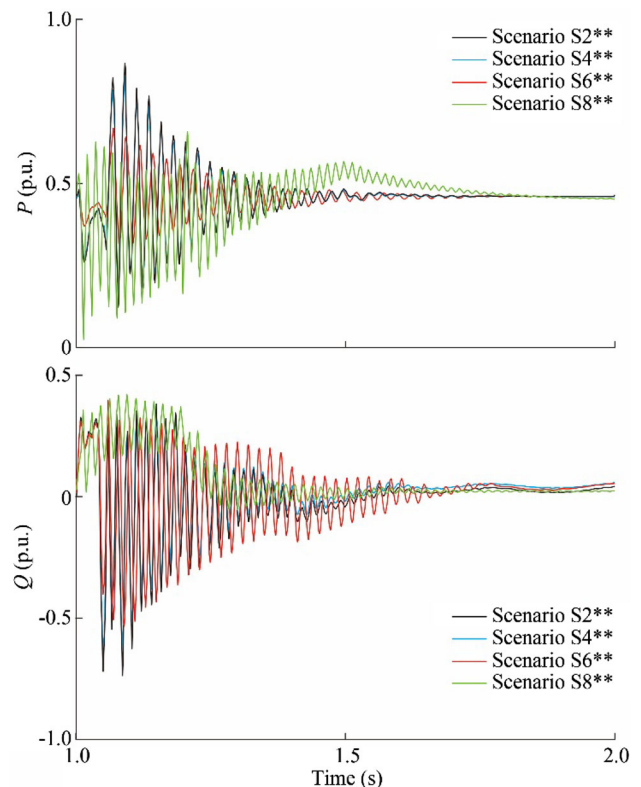


**Fig. 24** Active and reactive power components of the aggregated WT in scenarios S2\*\*, S4\*\*, S6\*\* and S8\*\*



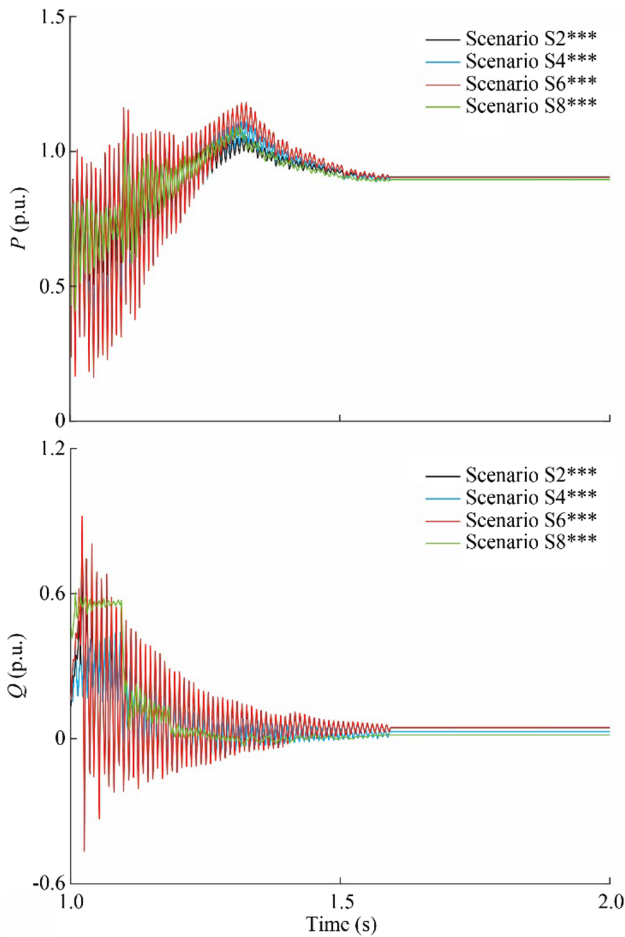


**Fig. 25** Active and reactive power components of the aggregated WT in scenarios S2\*\*\*, S4\*\*\*, S6\*\*\* and S8\*\*\*

fulfill the grid code requirement regarding FRT. The desired FRT operation of DFIG is achieved by limiting the output signals of the damping controller dynamically to avoid saturating the DFIG converters. Like the simple linearized model used in damping controller design, the WFC is considered in the EMT simulation model.

The EMT simulation results confirm the effectiveness of the proposed SSI damping controller for a wide range of the frequencies of the SSI mode resulting from various wind farm operation conditions and transmission line outage scenarios. The EMT simulation results also confirm the grid compliant operation of the DFIG.

**Acknowledgements** This work was supported by Canadian Network for Research and Innovation in Machining Technology and Natural Sciences and Engineering Research Council of Canada (No. 10.13039/501100000038).

**Open Access** This article is distributed under the terms of the Creative Commons Attribution 4.0 International License (<http://creativecommons.org/licenses/by/4.0/>), which permits unrestricted use, distribution, and reproduction in any medium, provided you give appropriate credit to the original author(s) and the source, provide a link to the Creative Commons license, and indicate if changes were made.

### Appendix A

The values of the SSI modes are shown in Tables A1–A4.

**Table A1** Impact of variations in  $R$  and wind speed on SSI mode shown in Fig. 8

$R$ (p.u.)	$W$ (p.u.)				
	0.6	0.7	0.8	0.9	1.0
0.0100	$3.13 + j268.3$	$2.62 + j266.4$	$2.10 + j264.5$	$1.54 + j262.6$	$0.96 + j260.7$
0.0138	$2.03 + j268.0$	$1.47 + j266.1$	$0.89 + j264.3$	$0.29 + j262.4$	$-0.35 + j260.5$
0.0175	$0.92 + j267.8$	$0.32 + j265.9$	$-0.31 + j264.1$	$-0.98 + j262.2$	$-1.68 + j260.3$
0.0213	$-0.19 + j267.6$	$-0.85 + j265.7$	$-1.53 + j263.9$	$-2.25 + j262.0$	$-3.01 + j260.1$
0.0250	$-1.31 + j267.4$	$-2.02 + j265.5$	$-2.76 + j263.7$	$-3.53 + j261.8$	$-4.35 + j260.0$
0.0288	$-2.45 + j267.2$	$-3.21 + j265.3$	$-4.00 + j263.5$	$-4.83 + j261.7$	$-5.70 + j259.8$
0.0325	$-3.59 + j267.0$	$-4.40 + j265.2$	$-5.24 + j263.3$	$-6.13 + j261.5$	$-7.06 + j259.7$
0.0363	$-4.73 + j266.8$	$-5.60 + j265.0$	$-6.50 + j263.2$	$-7.44 + j261.4$	$-8.42 + j259.6$
0.0400	$-5.89 + j266.7$	$-6.81 + j264.8$	$-7.76 + j263.0$	$-8.76 + j261.2$	$-9.80 + j259.5$

**Table A2** Impact of variations in  $X_L$  and wind speed on SSI mode shown in Fig. 9

$X_L$ (p.u.)	$W$ (p.u.)				
	0.6	0.7	0.8	0.9	1.0
0.400	$-0.59 + j263.9$	$-1.33 + j261.8$	$-2.11 + j259.7$	$-2.93 + j257.6$	$-3.80 + j255.5$
0.425	$-0.93 + j265.7$	$-1.66 + j263.7$	$-2.41 + j261.7$	$-3.21 + j259.7$	$-4.05 + j257.7$
0.450	$-1.23 + j267.3$	$-1.94 + j265.4$	$-2.68 + j263.6$	$-3.45 + j261.7$	$-4.26 + j259.9$
0.475	$-1.50 + j268.9$	$-2.18 + j267.2$	$-2.90 + j265.4$	$-3.64 + j263.7$	$-4.43 + j261.9$
0.500	$-1.73 + j270.5$	$-2.40 + j268.8$	$-3.09 + j267.1$	$-3.81 + j265.5$	$-4.56 + j263.9$
0.525	$-1.94 + j272.0$	$-2.58 + j270.4$	$-3.25 + j268.8$	$-3.95 + j267.3$	$-4.67 + j265.7$
0.550	$-2.12 + j273.4$	$-2.74 + j271.9$	$-3.39 + j270.4$	$-4.06 + j268.9$	$-4.76 + j267.5$
0.575	$-2.28 + j274.8$	$-2.88 + j273.4$	$-3.51 + j271.9$	$-4.15 + j270.5$	$-4.82 + j269.2$
0.600	$-2.42 + j276.1$	$-3.00 + j274.7$	$-3.61 + j273.4$	$-4.23 + j272.1$	$-4.88 + j270.8$

**Table A3** Impact of variations in  $X_C$  and wind speed on SSI mode shown in Fig. 10

$X_C$ (p.u.)	$W$ (p.u.)				
	0.6	0.7	0.8	0.9	1.0
0.50	$-3.98 + j282.8$	$-4.64 + j281.3$	$-5.32 + j279.9$	$-6.02 + j278.4$	$-6.75 + j277.0$
0.55	$-3.22 + j278.3$	$-3.89 + j276.7$	$-4.59 + j275.2$	$-5.31 + j273.6$	$-6.07 + j272.1$
0.60	$-2.47 + j274.1$	$-3.16 + j272.4$	$-3.87 + j270.7$	$-4.61 + j269.0$	$-5.39 + j267.4$
0.65	$-1.73 + j270.0$	$-2.43 + j268.2$	$-3.16 + j266.4$	$-3.92 + j264.6$	$-4.71 + j262.9$
0.70	$-1.00 + j266.1$	$-1.71 + j264.2$	$-2.45 + j262.3$	$-3.22 + j260.4$	$-4.04 + j258.5$
0.75	$-0.27 + j262.4$	$-0.99 + j260.4$	$-1.74 + j258.3$	$-2.52 + j256.3$	$-3.36 + j254.4$
0.80	$0.45 + j258.8$	$-0.27 + j256.7$	$-1.03 + j254.5$	$-1.83 + j252.4$	$-2.68 + j250.3$

**Table A4** Impact of wind turbine outages and wind speed on SSI mode shown in Fig. 11

Number of WTs	$W$ (p.u.)				
	0.6	0.7	0.8	0.9	1.0
50	$0.76 + j236.3$	$-0.15 + j234.1$	$-1.13 + j231.8$	$-2.18 + j229.5$	$-3.32 + j227.2$
100	$1.41 + j245.5$	$0.57 + j243.1$	$-0.31 + j240.6$	$-1.27 + j238.2$	$-2.31 + j235.7$
150	$1.54 + j255.3$	$0.79 + j252.8$	$-0.02 + j250.3$	$-0.87 + j247.7$	$-1.80 + j245.2$
200	$0.91 + j269.4$	$0.24 + j267.0$	$-0.47 + j264.5$	$-1.22 + j262.1$	$-2.02 + j259.6$
266	$-1.70 + j293.0$	$-2.33 + j290.9$	$-2.99 + j288.7$	$-3.68 + j286.6$	$-4.41 + j284.5$

## References

- [1] Bozhko S, Blasko-Gimenez R, Li R et al (2007) Control of offshore DFIG-based wind farm grid with line-commutated HVDC connection. *IEEE Trans Energy Convers* 22(1):71–78
- [2] Fan L, Zhu C, Miao Z et al (2011) Modal analysis of a DFIG-based wind farm interfaced with a series compensated network. *IEEE Trans Energy Convers* 26(4):1010–1020
- [3] Sahni M, Badrzadeh B, Muthumuni D et al (2012) Sub-synchronous interaction in wind power plants part II: an ERCOT case study. In: *Proceedings of IEEE PES general meeting, San Diego, USA, 22–26 July 2012*, 9 pp
- [4] Adams J, Carter J, Huang S (2012) ERCOT experience with sub-synchronous control interaction and proposed remediation. In: *Proceedings of IEEE PES transmission and distribution conference and exposition, Orlando, USA, 7–10 May 2012*, 5 pp
- [5] Virulkar V, Gotmare G (2016) Sub-synchronous resonance in series compensated wind farm: a review. *Renew Sustain Energy Rev* 55:1010–1029
- [6] Leon A, Solsona J (2015) Sub-synchronous interaction damping control for DFIG wind turbines. *IEEE Trans Power Syst* 30(1):419–428
- [7] Karaagac U, Faried S, Mahseredjian J et al (2014) Coordinated control of wind energy conversion systems for mitigating sub-synchronous interaction in DFIG-based wind farms. *IEEE Trans Smart Grid* 5(5):2440–2449



- [8] Chowdhury M, Mahmud M, Shen W et al (2017) Nonlinear controller design for series-compensated DFIG-based wind farms to mitigate subsynchronous control interaction. *IEEE Trans Energy Convers* 32(2):707–719
- [9] Ghafouri M, Karaagac U, Karimi H et al (2017) An LQR controller for damping of subsynchronous interaction in DFIG-based wind farms. *IEEE Trans Power Syst* 32(6):4934–4942
- [10] Ghafouri M, Karaagac U, Mahseredjian J et al (2019) SSCI damping controller design for series compensated DFIG based wind parks considering implementation challenges. *IEEE Trans Power Syst*. <https://doi.org/10.1109/tpwrs.2019.2891269>
- [11] Huang PH, Moursi MSE, Xiao W et al (2015) Subsynchronous resonance mitigation for series-compensated DFIG-based wind farm by using two-degree-of-freedom control strategy. *IEEE Trans Power Syst* 30(3):1442–1454
- [12] Fan L, Miao Z (2012) Mitigating SSR using DFIG-based wind generation. *IEEE Trans Sustain Energy* 3(3):349–358
- [13] Chhabra M, Barnes F (2014) Robust current controller based solar-inverter system used for voltage regulation at a substation. In: *Proceedings of IEEE 40th photovoltaic specialist conference*, Denver, USA, 8–13 June 2014, 6 pp
- [14] Bevrani H, Feizi M, Ataei S (2016) Robust frequency control in an islanded microgrid:  $H_\infty$  and  $\mu$  synthesis approaches. *IEEE Trans Smart Grid* 7(2):706–717
- [15] Li J, Zhang XP (2016) Impact of increased wind power generation on subsynchronous resonance of turbine-generator units. *J Mod Power Syst Clean Energy* 4(2): 219–228
- [16] Karaagac U, Saad H, Peralta J et al (2015) Doubly-fed induction generator-based wind park models in EMTP-RV. Polytechnique Montréal, Canada
- [17] Netz GmbH EON (2006) Grid code—high and extra high voltage. Bayreuth, Germany
- [18] Zhou K, Doyle J (1998) *Essentials of robust control*. Prentice Hall, Upper Saddle
- [19] Chilali M, Gahinet P, Apkarian P (1999) Robust pole placement in LMI regions. *IEEE Trans Autom Control* 44(12):2257–2270
- [20] Gu D, Petkov P, Konstantinov M (2005) *Robust control design with MATLAB*. Springer, London
- [21] Mahseredjian J, Dennetière S, Dubé L et al (2007) On a new approach for the simulation of transients in power systems. *Electr Power Syst Res* 77(11):1514–1520
- [22] Haddadi A, Kocar I, Kauffmann T et al (2019) Field validation of generic wind park models using fault records. *J Mod Power Syst Clean Energy* 7(4): 826–836

Iran, in 2009 and 2011, respectively. He obtained his Ph.D. degree from Ecole Polytechnique de Montreal, Canada, in 2018. He is currently working at Concordia University as postdoctoral researcher. His research interests include microgrid, wind energy, and application of robust control in power systems.

**Ulas KARAAGAC** received the B.Sc. and M.Sc. degrees in electrical and electronics engineering from Middle East Technical University, Ankara, Turkey in 1999 and 2002, respectively, and the Ph.D. degree in electrical engineering from Ecole Polytechnique de Montreal, Canada in 2011. He worked as an R&D engineer at TUBITAK-BILTEN, Turkey from 1999 to 2007. He was Ph.D. scholar between 2007 and 2011 and worked as research associate between 2012 and 2016 at Ecole Polytechnique de Montreal. He joined the Department of Electrical Engineering of the Hong Kong Polytechnic University as Research Assistant Professor in December 2016. His research interests areas include integration of large-scale renewables into power grids, HVDC transmission, modeling and simulation of large-scale power systems, and power system dynamics and control.

**Houshang KARIMI** received the B.Sc. and M.Sc. degrees from Isfahan University of Technology, Isfahan, Iran, in 1994 and 2000, respectively, and the Ph.D. degree from the University of Toronto, Toronto, Canada, in 2007, all in electrical engineering. He was a postdoctoral Fellow in the Department of Electrical and Computer Engineering, University of Toronto from 2007 to 2008. He was with the Department of Electrical Engineering, Sharif University of Technology, Tehran, Iran, from 2009 to 2012. From June 2012 to January 2013, he was a Visiting Researcher in the ePower lab of the Department of Electrical and Computer Engineering, Queens University, Kingston, Canada. He joined the Department of Electrical Engineering, Ecole Polytechnique de Montreal, Canada, in 2013, where he is currently an Assistant Professor. His research interests include control systems, distributed generations, and microgrid control.

**Jean MAHSEREDJIAN** received the M.A.Sc. and Ph.D. degrees in Ecole Polytechnique de Montreal, Canada, in 1985 and 1991, respectively. From 1987 to 2004, he was with IREQ (Hydro Quebec), working on research and development activities related to the simulation and analysis of electromagnetic transients. In December 2004, he joined the Faculty of Electrical Engineering at Ecole Polytechnique de Montreal, where he is currently a Professor.

**Mohsen GHAFOURI** received the B.Sc. and M.Eng. degrees in electrical engineering from Sharif University of Technology, Tehran,